

PAPER

## Absolute keV x-ray yield and conversion efficiency in over dense Si sub-petawatt laser plasma

To cite this article: Sergey N Ryazantsev *et al* 2022 *Plasma Phys. Control. Fusion* **64** 105016

View the [article online](#) for updates and enhancements.

### You may also like

- [Laser-generated supersonic plasma jets and shocks in a transverse magnetic field](#)  
H Bohlin, F-E Brack, M Cervenak *et al.*
- [Accelerating the rate of discovery: toward high-repetition-rate HED science](#)  
T Ma, D Mariscal, R Anirudh *et al.*
- [Experimental study of strongly mismatched regime of laser-driven wakefield acceleration](#)  
S E Perevalov, K F Burdonov, A V Kotov *et al.*



**IOP | ebooks™**

Bringing together innovative digital publishing with leading authors from the global scientific community.

Start exploring the collection—download the first chapter of every title for free.

# Absolute keV x-ray yield and conversion efficiency in over dense Si sub-petawatt laser plasma

Sergey N Ryazantsev<sup>1,2,\*</sup> , Artem S Martynenko<sup>2,3</sup> , Maksim V Sedov<sup>2</sup>,  
Igor Yu Skobelev<sup>1,2</sup> , Mikhail D Mishchenko<sup>2,4</sup>, Yaroslav S Lavrinenko<sup>2,5</sup> ,  
Christopher D Baird<sup>6</sup> , Nicola Booth<sup>7</sup>, Phil Durey<sup>6</sup>, Leonard N K Döhl<sup>6</sup>, Damon Farley<sup>6</sup>,  
Kathryn L Lancaster<sup>6</sup>, Paul McKenna<sup>8</sup> , Christopher D Murphy<sup>6</sup> , Tatiana A Pikuz<sup>2,9</sup>,  
Christopher Spindloe<sup>7</sup>, Nigel Woolsey<sup>6</sup>  and Sergey A Pikuz<sup>1,2</sup> 

<sup>1</sup> National Research Nuclear University MEPhI (Moscow Engineering Physics Institute), 115409 Moscow, Russia

<sup>2</sup> Joint Institute for High Temperatures of the Russian Academy of Sciences, Moscow 125412, Russia

<sup>3</sup> Plasma Physics Department, GSI Helmholtzzentrum für Schwerionenforschung, 64291 Darmstadt, Germany

<sup>4</sup> European XFEL, 22869 Schenefeld, Germany

<sup>5</sup> Moscow Institute of Physics and Technology, State University, 141701 Moscow, Russia

<sup>6</sup> Department of Physics, York Plasma Institute, University of York, York YO10 5DD, United Kingdom

<sup>7</sup> Central Laser Facility, STFC Rutherford Appleton Laboratory, Didcot OX11 0QX, United Kingdom

<sup>8</sup> Department of Physics, SUPA, University of Strathclyde, Glasgow G4 0NG, United Kingdom

<sup>9</sup> Institute for Open and Transdisciplinary Research Initiatives, Osaka 565-0871, Japan

E-mail: [SNRyazantsev@mephi.ru](mailto:SNRyazantsev@mephi.ru)

Received 1 February 2022, revised 12 July 2022

Accepted for publication 19 August 2022

Published 7 September 2022



## Abstract

Laser-produced plasmas are bright, short sources of x-rays commonly used for time-resolved imaging and spectroscopy. Their usage implies accurate knowledge of laser-to-x-ray conversion efficiency (CE), spectrum, photon yield and angular distribution. Here, we report on soft x-ray emission in the direction close to the target normal from a thin Si foil irradiated by a sub-PW picosecond laser pulse. These absolute measurements cover a continuous and broad spectral range that extends from 4.75 to 7.3 Å (1.7–2.6 keV). The x-ray spectrum consists of spectral line transitions from highly charged ions and broadband emission with contributions from recombination and free-free processes that occur when electrons decelerate in plasma electromagnetic fields. Angular distribution of the emission was investigated via particle-in-cell simulations, which allowed to estimate the yield into the full solid angle. We find that experimental and simulation estimations of laser to free-free emission CE are in good agreement.

**Keywords:** PW laser plasma, absolute emissivity of laser plasma, crystal x-ray spectrometer, laser to x-rays conversion efficiency

(Some figures may appear in colour only in the online journal)

\* Author to whom any correspondence should be addressed.

## 1. Introduction

Plasmas produced by irradiation of different objects (flat foils [1–3], microstructured surfaces [4, 5], wavelength-scale spheres [6], velvet surfaces [7], nanowires [8, 9], gas jets [10–12]) by intense laser pulses (Laser Produced Plasma, referred below as LPP) are widely used as an x-rays sources for both fundamental and applied research.

This is due to the possibility to precisely synchronise a measurement with phase of evolution of a probed object and the relatively short duration of the emission. When nanosecond pulses are used, it is usually equal to their duration [13] and, in the case of picosecond pulses, exceeds it not by more than two orders of magnitude depending on laser intensity [1] or target type [7]. It should be noted, however, that the radiation from plasma sources generated by femtosecond pulses also can last up to several picoseconds [14]. Broadband emission sources are often needed for bioimaging and absorption spectroscopy. LPP at the table-top scale are used as x-ray sources in commercial applications [15] and at the very large scale in inertial confinement fusion (ICF) research as very bright x-ray backlighters for capsule explosions. Petawatt-class (PW) laser facilities (such as ARC [16] and PETAL [17] or others mentioned at table E.1 in [18]) which can produce picosecond pulses of about kJ are used for these purposes. Even for ICF experiments, sources of soft x-rays are required. For example, low energy photons of  $<2$  keV are used for the backlighting of direct-drive cryogenic DT implosions [19] due to the low opacity of the plastic shell and the deuterium-tritium fuel [20]. In addition, the low energy part of the spectrum of PW short-duration plasma sources is used to study warm-dense-matter by absorption spectroscopy [21].

These two applications, the imaging of an ICF experiment and diagnosis of warm-dense-matter, require a different spectral composition of the probe radiation. A source with a narrow emission band, ideally monochromatic, is required to acquire high-quality backlit images. Absorption spectroscopy, on the other hand, is most effective when using a radiation source with a continuous spectrum without spectral line features or sharp drops in intensity [22]. Both types of the probe radiation can be obtained using LPP due to different processes, which are shown in figure 1.

Plasma ions produce characteristic spectral lines during transitions of electrons between bound energy levels. For highly charged ions even with relatively low- $Z$  (around 10) the lines are in the keV range of photon energy. Usually transitions from the excited state with principal quantum number  $n = 2$  to the ground state in hydrogen-like ( $\text{Ly}_\alpha$ ) and helium-like transition ( $\text{He}_\alpha$ ) is at the appropriate wavelength for high-contrast quasi-monochromatic backlighting imaging [20, 23]. The plasma spectrum also contains lower intensity continuous emission from free-bound (photorecombination) and free-free (bremsstrahlung and synchrotron emission) transitions. Contributions of the individual process depend on element and irradiation conditions. Therefore a significant experimental effort is required to characterize

LPP sources including those produced by picosecond PW pulses.

In this work we investigate the soft x-ray emission properties of a near solid density plasma generated in a Si foil by a sub-PW laser pulse. The aim of the work is to present exact values for the x-ray source photon yield in absolute units in the direction close to the target normal and briefly describe physical processes that contribute to the emission.

## 2. Experimental setup

The experimental investigation of the emissivity in soft x-ray range as a relativistic-intensity picosecond duration laser pulse strikes a Si foil was performed at the Vulcan PW laser facility [24]. A schematic representation of the experimental setup is shown in figure 1. The plasma was created by irradiating  $2\text{ }\mu\text{m}$  thick Si foils by pulses of p-polarised laser radiation with wavelength  $\lambda = 1.054\text{ }\mu\text{m}$ . Duration of the pulses was  $\tau = 1$  ps. The beam was focused by an off-axis parabolic mirror to a spot with a diameter of  $\approx 7\text{ }\mu\text{m}$ . Initial (measured before the compressor) energy of the used pulses was  $\approx 350$  J, but only about 60% ( $\approx 210$  J) of it reached the target surface due to losses in different parts of the beam optical path including a plasma mirror [25] applied to enhance the laser pulse temporal contrast. The indicated parameters values corresponds to the pulse power  $P = 0.2$  PW and intensity  $I = 3 \times 10^{20}\text{ W cm}^{-2}$ .

X-rays emitted from the front of the target during one laser shot was registered with three focusing spectrometers with spatial resolution (FSSR) [26] installed in directions close to the surface normal. Spherically bent  $\alpha$ -quartz crystals with Miller indexes ( $hkl$ ) (100) (interplanar spacing  $2d = 8.512\text{ }\text{\AA}$ ) and (101) ( $2d = 6.666\text{ }\text{\AA}$ ) were used as disperse elements for them. Two FSSRs with the (100) crystals observed the overlapping wavelength ranges  $5\text{--}6.8$  and  $6.5\text{--}7.3\text{ }\text{\AA}$ . The third one with the (101) crystal was aligned to register photons with wavelength from  $4.75$  to  $6\text{ }\text{\AA}$ . Dispersion schemes chosen for the spectrometers provided spectral and spatial resolution of  $\lambda/\Delta\lambda \approx 0.5 \times 10^4$  and  $\Delta X \approx 100\text{ }\mu\text{m/pixel}$  correspondingly. All the spectrometers were shielded against spurious radiation generated by the electrons from the interaction point as they hit the chamber walls, optical posts, and so on. Two of the FSSRs were in housings made of  $5\text{ mm}$  lead with small windows in the direction of the target crystal. The third FSSR was installed in a separate vacuum chamber connected to the main chamber by a narrow tube with its axis oriented towards the target. Also,  $0.5\text{ T}$  neodymium-iron-boron permanent magnets were installed between the FSSR crystals and the interaction point. As a result, the electrons accelerated towards the crystals could not reach them if their kinetic energy was less than  $50\text{ MeV}$ . Fujifilm BAS-TR image plates (IPs) and Andor CCD DX-434 (only for one of the spectrometers) were used as x-ray detectors. The IPs were covered by two layers of  $1\text{ }\mu\text{m}$  thick polypropylene ( $\text{C}_3\text{H}_6$ )<sub>n</sub> with a thin ( $0.2\text{ }\mu\text{m}$ ) layer of Al evaporated on it or by  $25\text{ }\mu\text{m}$  thick beryllium film. The CCD sensor was shielded by a  $25\text{ }\mu\text{m}$  Be foil for all the shots. The slits of

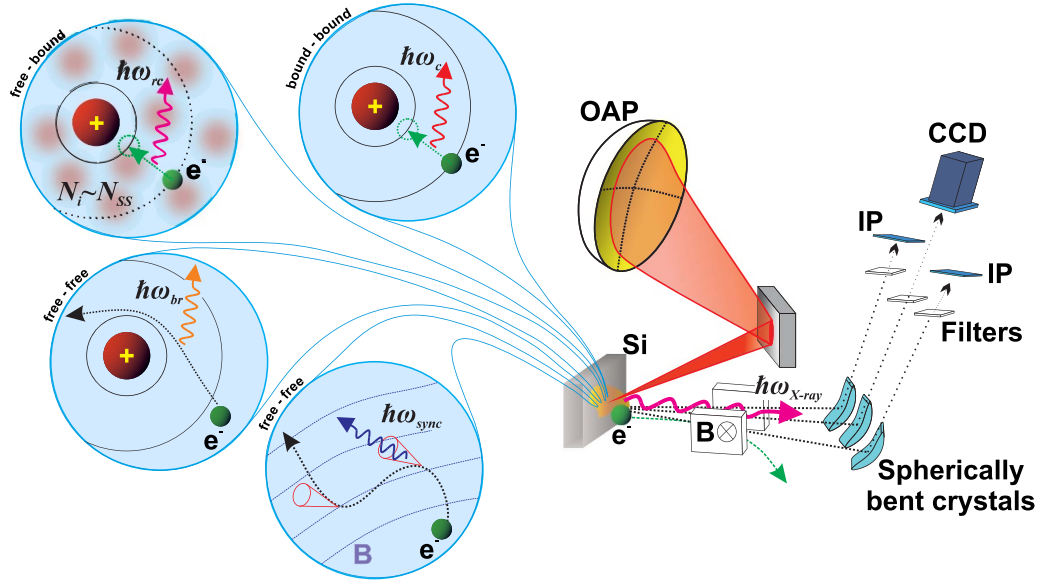


**Figure 1.** Experimental setup and schematic of the processes that form the shape of the plasma soft x-ray radiation spectrum registered in the experiment.

the magnets were also covered by a single layer of 5  $\mu\text{m}$  Mylar ( $\text{C}_{10}\text{H}_8\text{O}_4$ ) to avoid detector saturation.

The spectrometers observation ranges overlap to provide cross-calibration between the FSSRs. This enabled the measurement of continuous and high-resolution spectra over photon wavelengths from 4.75 to 7.3  $\text{\AA}$  (1.7 to 2.6 keV). The raw spectra normalized to maximum intensity registered by the individual FSSR spectrometers are shown in figure 2(a).

All data registered with the FSSRs were corrected for filtering, crystal reflectivity and detector response functions. Reflectivity was calculated by numerical modelling as described in [27] by ray tracing through the spectrometer. The actual crystallographic rocking curves of the spherically bent crystals installed in the FSSRs were used for it. They were calculated with the software XOP [28] and presented in appendix together with sensitivity functions of the IPs. Transmission functions for the filters foils were calculated using the Henke tables [29]. A summary of the response functions for each spectrometer is shown in figure 2(b). After convolution of the registered signal with them an initial plasma radiation spectrum shape was restored (figure 2(c)). Consideration of the equipment response function allowed to scale the intensity (vertical axis in the figure) in absolute units of photons  $\text{\AA}^{-1} \text{sr}^{-1}$ . Thus it represents the emissivity of the source radiation in the direction of the spectrometers crystals (close to the targets normal). The most significant corrections were needed around the Si K-edge at 6.7135  $\text{\AA}$  [30]. This causes a drop in reflectivity of the  $\alpha$ -quartz ( $\text{SiO}_2$ ) crystals in the wavelength range close to the  $\text{He}_\alpha$  line.

### 3. Discussion

The spectrum shown in figure 2(c) contains both characteristic and continuous emission components. Its shape is formed by

all types of electron transitions: free-free, free-bound, bound-bound (figure 1). The characteristic emission of plasma ions is produced by transitions between energy states of H- and He-like Si ions. All the corresponding spectral lines are broadened due to the strong Stark effect. Their experimental shape is correctly reproduced (figure 3) by a theoretical spectrum simulated for the plasma electron temperature  $T_e = 650 \text{ eV}$  and electron density of  $4 \times 10^{23} \text{ cm}^{-3}$ , which is about 60% of Si solid density value  $N_{ss} \approx 6 \times 10^{23} \text{ cm}^{-3}$ . It was achieved due to the extremely high value of the laser pulse temporal contrast of  $10^{10}$  additionally enhanced by the plasma mirror.

The most intense line is the  $\text{Ly}_\alpha$  ( $2p \rightarrow 1s$  transition in an H-like ion). Emissivity of the source in this line (the narrow wavelength range from 6.05 to 6.35  $\text{\AA}$ , 1.95–2.05 keV, which contains the line itself and its dielectronic satellites) in the direction close to the targets normal is about  $1.7 \times 10^{13} \text{ photons sr}^{-1}$ . This part of the plasma spectrum is best suited for implementation of quasi-monochromatic backlights schemes. The value for the broad peak indicated in the figure as  $\text{He}_\alpha$  (range from 6.53 to 6.89  $\text{\AA}$ , 1.8–1.9 keV) is  $\approx 0.8 \times 10^{13} \text{ photons sr}^{-1}$ . In fact, this spectral region contains overlapping  $\text{He}_\alpha$  ( $1s2p \ ^1P_1 \rightarrow 1s^2 \ ^1S_0$  in He-like ions), intercombination line ( $1s2p \ ^3P_{2,1} \rightarrow 1s^2 \ ^1S_0$ ) and dielectronic satellites emitted by Li-like ions. Note that the peak to the left of the intensity drop caused by the K-edge is not the intercombination line. This is an artefact of registration previously observed for the spectrometers used in the experiment. Emissivities of the source in the  $\text{Ly}_\beta$  ( $3p \rightarrow 1s$ ) and  $\text{He}_\beta$  ( $1s3p \ ^1P_1 \rightarrow 1s^2 \ ^1S_0$ ) lines are  $0.4 \times 10^{13}$  and  $0.6 \times 10^{13} \text{ photons sr}^{-1}$  respectively. In comparison the  $\text{K}_\alpha$  line at 7.12  $\text{\AA}$  is weak as most of the Si is highly ionised. The indicated numbers correspond to a conversion efficiency (CE) of laser pulse energy to  $\text{He}_\alpha$ ,  $\text{Ly}_\alpha$ ,  $\text{Ly}_\beta$ ,  $\text{He}_\beta$  lines emission in the direction close to the target normal as  $\approx 1.2 \times 10^{-5} \text{ sr}^{-1}$ ,

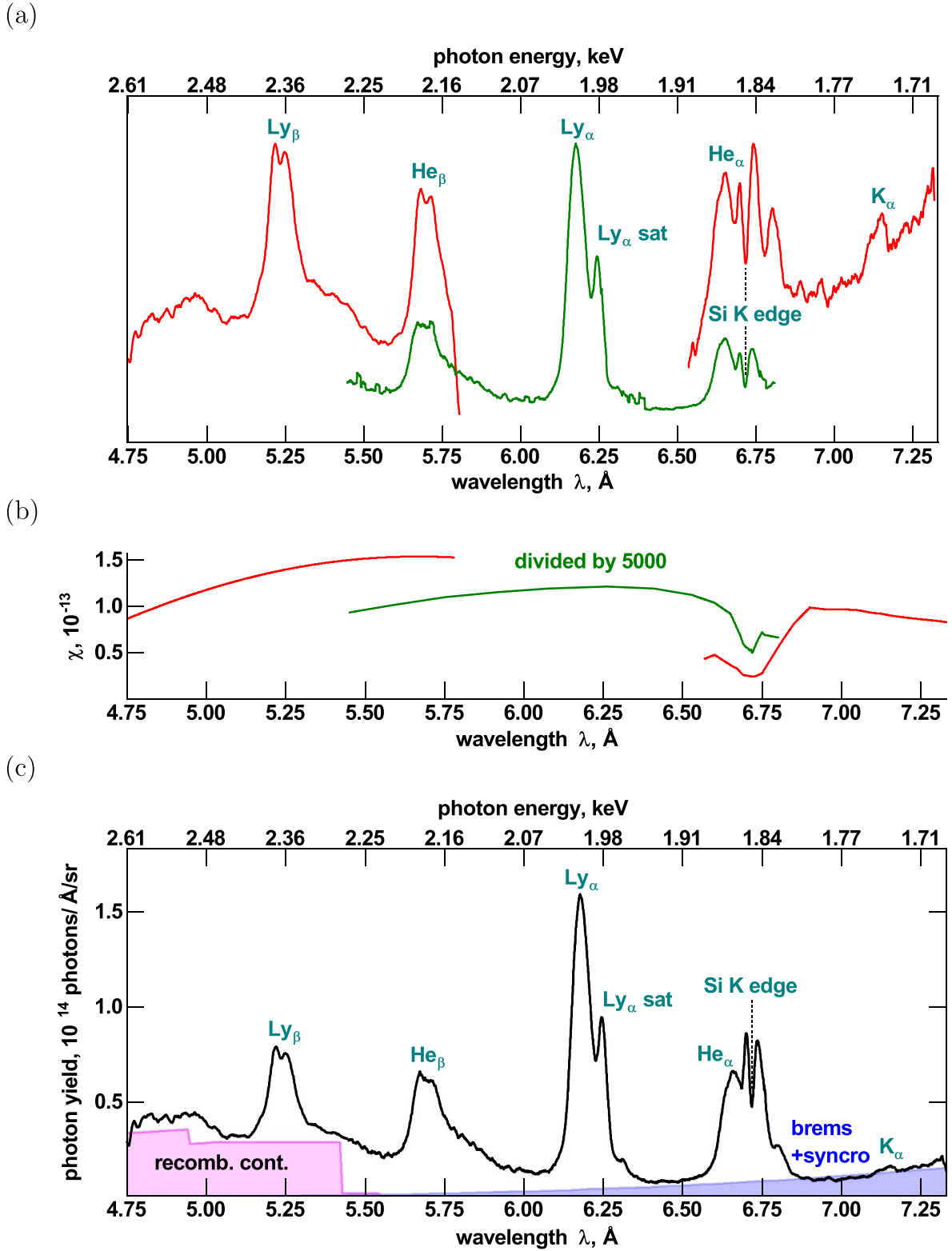


**Figure 2.** (a)—Normalized experimental emission spectra registered by the FSSRs from the front side of Si foil before convolution with the spectrometer route response functions  $\chi(\lambda)$  shown in (b)— $\chi(\lambda)$  is a ratio of the number of registered photons of  $\lambda$  wavelength to the one emitted by the source. (c)—Combined experimental emission spectrum after convolution with  $\chi(\lambda)$ . The blue and purple polygons qualitatively demonstrate contributions of bremsstrahlung, synchrotron emission and recombination continuum. Shape of the latter one was calculated for solid-state Si plasma ( $N_i = 6 \times 10^{22} \text{ cm}^{-3}$ ).

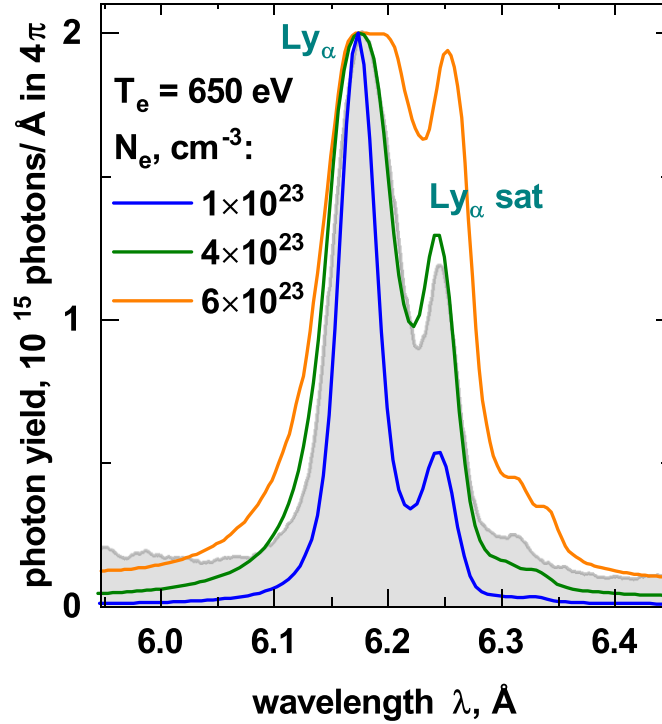


**Figure 3.** Comparison of  $\text{Ly}_\alpha$  line shape registered in the experiment with that calculated theoretically for the fixed electron temperature  $T_e = 650$  eV and different electron densities:  $N_e = 1 \times 10^{23}$  (blue line),  $4 \times 10^{23}$  (green) and  $6 \times 10^{23} \text{ cm}^{-3}$  (orange). For the calculations it was assumed that the plasma has a linear size of  $3 \mu\text{m}$ . The simulated spectra were obtained with PrismSPECT software [31].

$\approx 2.5 \times 10^{-5} \text{ sr}^{-1}$ ,  $\approx 0.75 \times 10^{-5} \text{ sr}^{-1}$ ,  $\approx 1.0 \times 10^{-5} \text{ sr}^{-1}$  respectively.

In the short wavelength part of the spectrum there is a pedestal. It results from the recombination continuum produced by free-bound transitions of plasma electrons. Spectral lines corresponding to  $4p \rightarrow 1s$  transitions in H- and He-like ions should be registered in this range, but they are suppressed due to ionization potential depression [32] in the dense plasma. The shape of the recombination continuum calculated using the Hummer–Mihalas [33] model for He- and H-like ions in a solid-density Si plasma is shown in figure 2(c) by the magenta area. Simulations indicate that the recombination continuum extends to  $2 \text{ \AA}$ . Quite high yield (average value is  $\approx 3 \times 10^{13} \text{ photons \AA}^{-1} \text{ sr}^{-1}$ ) value and absence of any spectral lines makes the recombination continuum part of the spectrum very suitable for x-ray absorption spectroscopy in the range  $\leq 5 \text{ \AA}$ .

Another part of the continuous emission arose from free-free processes. They contribute to the spectrum through a monotonic growth in intensity in the long wavelength part. It is approximated by an exponential function shown by the blue line in figure 2(c). An area under this curve gives an estimation for an amount of energy associated with free-free emission is  $E_{\text{cont}} = 5 \text{ mJ sr}^{-1}$ , which corresponds to CE of  $2.5 \times 10^{-5} \text{ sr}^{-1}$ .

It is also possible to estimate a ratio  $\text{CE}_{4\pi}$  of the energy emitted in the full solid angle  $4\pi$  to the energy of the incident laser pulse. For bremsstrahlung and synchrotron emission it can be done semi-analytically on the basis of electron energy distribution numerically obtained by particle-in-cell

(PIC) simulations. We have performed two-dimensional (2D) PIC simulation via the EPOCH [34] code.

All the modelling parameters were chosen close to experimental conditions: laser wavelength  $\lambda_{\text{laser}} = 1.054 \mu\text{m}$ , focal spot radius  $4 \mu\text{m}$ , angle of incidence  $\alpha = 45^\circ$ , intensity  $I_{\text{las}} = 3 \times 10^{20} \text{ W cm}^{-2}$ . The laser pulse had Gaussian spatial and 3rd order super-Gauss temporal profile (figure 4(a)). A  $2 \mu\text{m}$  thick layer of fully ionized Si ions with solid-state density ( $5 \times 10^{22} \text{ ions cm}^{-3}$ ) was used as a target. A long laser pulse requires a large simulation box to accurately describe the laser-target interaction and to accommodate the expanding plasma. In our simulations the box size was  $120 \times 120 \mu\text{m}$  with  $10 \times 10 \text{ nm}$  grid. The simulation included a current smoothing algorithm and third order particle weighting to limit noise and numerical heating. All boundary conditions were absorbing for radiation and thermalizing for particles.

For an accurate description of the interaction of a laser pulse with a solid target, it is necessary that the minimum achievable particle density in the calculation (1 macro particle in 1 cell) be less than the critical density. On the other hand, at the edge of the simulation area particles will never interact with the laser pulse. They are needed only to maintain the quasi-neutrality of the plasma via the return current. Specifying a large number of macro particles for all cells in the target is a waste of computational resources. Therefore, in order to save computational time, the target was conditionally divided into several zones (figure 4(b)). The central zone 1 had 50 macro ion particles and  $50 \times 14$  macro electron particles (1 macro electron in 1 cell corresponds to  $0.9 n_{\text{cr}}$ ) in each cell, zone 2 had half the number of macro particles in each cell (25 ions and



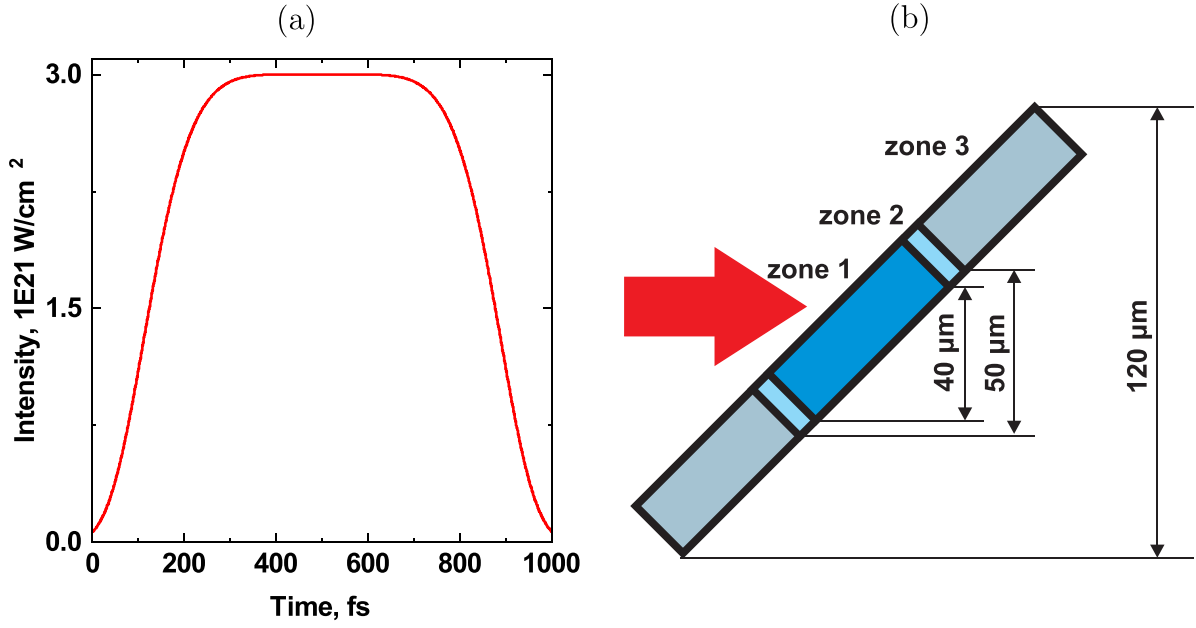


**Figure 4.** (a)—Temporal profile of the laser pulse used in PIC simulations. (b)—Scheme of dividing the target into zones with different numbers of macroparticles.

$25 \times 14$  electrons) and zone 3 had 10 macro ion particles and  $10 \times 14$  macro electron particles in each cell, respectively. The boundary of zone 1 was chosen from the condition that during the simulation time (1.1 ps) the electrons from zone 2 did not reach the focal spot.

The electron energy spectrum predicted by the PIC simulations is shown in figure 5(a). It can be roughly reproduced by a sum of three Maxwell distributions with temperatures of 5, 80 and 650 keV and electron densities  $N_e = 3 \times 10^{13}$ ,  $9 \times 10^{13}$ ,  $1.5 \times 10^{13} \text{ cm}^{-3}$  respectively. On the base of these values it is possible to estimate amount of energy emitted as Bremsstrahlung and synchrotron radiation using modified Kramers formula (1) from [35] and the classical expression (2) from [36] correspondingly:

$$dI_{\text{Brems}}(E) = C \frac{Z^2 N_i n_e}{\sqrt{T_e}} \exp\left(-\frac{E}{T_e}\right) dE; C = \frac{16}{3} \sqrt{\frac{2\pi}{0.5}} \frac{e^6}{m_e^{3/2} c^3}, \quad (1)$$

$$dI_{\text{synchro}}(E) = \frac{\sqrt{3}}{2\pi} \frac{e^3 H}{m_e c^2} F\left(\frac{E}{E_c}\right) dE; F(\xi) = \int_{\xi}^{\infty} K_{\frac{5}{3}}(\xi) d\xi, \quad (2)$$

where  $Z$ —atomic number of the target atoms,  $N_i$ —ion density ( $6 \times 10^{22} \text{ cm}^{-3}$ ),  $n_e$ —number of electrons,  $T_e$ —electron temperature in eV,  $g^{\text{ff}}$ —Gaunt factor,  $e$  and  $m_e$ —electron charge and mass,  $c$ —speed of light,  $H$ —magnetic field (considered as constant calculated as  $\sqrt{\frac{2I}{c}} = 4.5 \times 10^8 \text{ G}$ ),  $K$  is the modified Bessel function of the second type and  $E_c$  is an energy around which the emission of an electron with energy  $T_e$  is concentrated:

$$E_c = \hbar \omega_c; \omega_c = \frac{3eH}{2m_e c} \left( \frac{T_e}{m_e c^2} \right)^2. \quad (3)$$

It should be noted that according to (3) only electrons with energy  $\geq 6 \text{ MeV}$  make a significant contribution in the energy range detected by our spectrometers.

Integrating of (1) and (2) over the range of photon energies observed in the experiment gives the values of 0.1 and 0.3 J for the Bremsstrahlung and synchrotron emission, respectively. Dividing by the energy of the laser pulse used in the experiment (210 J) gives  $\text{CE}_{4\pi}$  values  $\eta_{\text{Brems}} = 3.3 \times 10^{-4}$  and  $\eta_{\text{synchro}} = 1 \times 10^{-3}$ . The EPOCH code itself is able to simulate spectrum (figure 5(b)) and angular distribution (figure 5(c)) of bremsstrahlung and synchrotron emission on the base of principles described in [37–39] and predict values for  $\text{CE}_{4\pi}$ . It gives  $\eta_{\text{Brems}}^{4\pi} = 3.4 \times 10^{-4}$  and  $\eta_{\text{synchro}}^{4\pi} = 1.3 \times 10^{-4}$ . Such a significant discrepancy for the synchrotron emission CEs is caused by using a fixed value of the magnetic field for the analytical estimation based on the equation (2).

The angular distribution predicted by PIC simulations (figure 5(c)) is not isotropic, because absorption within the target occurs in the direction parallel to the surface of the target ( $45^\circ$ – $235^\circ$  direction). The simulated distribution together with the experimental value for the energy of the emission associated with free-free transitions registered by the spectrometers allows to estimate the total energy emitted by the source in full solid angle  $4\pi$  as bremsstrahlung and synchrotron emission. The obtained values is  $E_{\text{cont}} \approx 33 \text{ mJ}$ , which is  $\approx 52\%$  of that obtained assuming an isotropic angular distribution. The corresponding  $\text{CE}_{4\pi}$  value is  $1.6 \times 10^{-4}$ , which is about three times less than predicted by the PIC simulation. Impacts of the two types of free-free emission are indistinguishable in the experimental spectrum. Therefore, it is impossible to give separate estimates for their CEs. Nevertheless, according to the PIC results synchrotron emission should be less intense than bremsstrahlung for all the directions and the  $E_{\text{cont}}$  is distributed between them as 1:2.6.

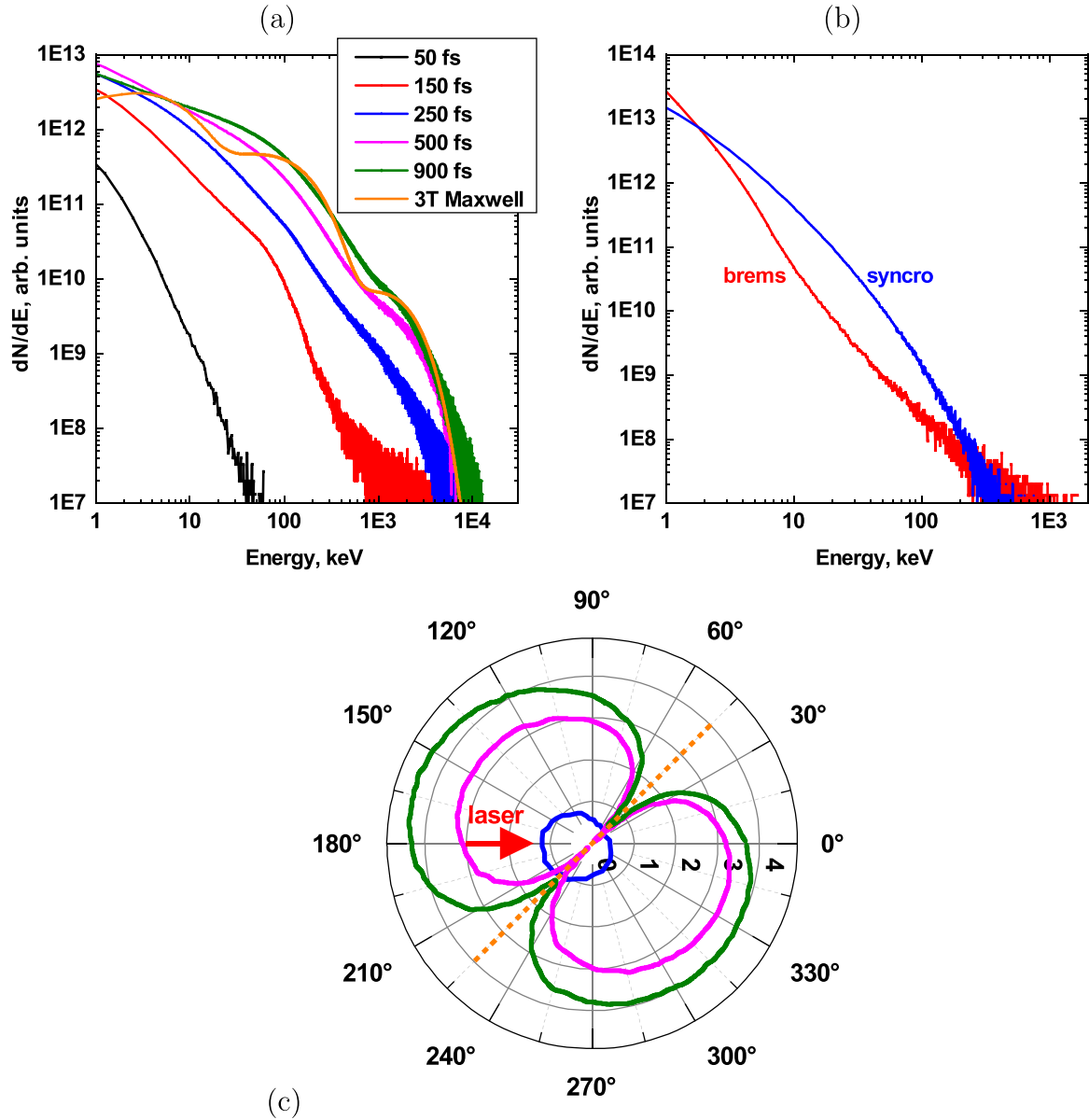


**Figure 5.** (a)—Electron energy distribution retrieved from PIC simulations for different moments of the laser-target interaction; (b)—spectra of bremsstrahlung and synchrotron emission retrieved from the PIC simulation; (c)—numerically calculated angular distribution of bremsstrahlung (magenta curve) and synchrotron radiation (blue) emitted in the 4.75–7.3 Å (1.7–2.6 keV) wavelength range by a 2  $\mu\text{m}$  thick layer of fully ionized Si ions with solid-state density irradiated by a subpicosecond laser pulse with intensity  $3 \times 10^{20} \text{ W cm}^{-2}$ . The solid green curve is the sum of two components.

It can be assumed that the angular distribution for the line emission of the source also has a ‘dipole’ shape. Under this assumption it is possible to estimate  $\text{CE}_{4\pi}$  in separate spectral lines. The values are  $\approx 0.8 \times 10^{-4}$ ,  $\approx 1.6 \times 10^{-4}$ ,  $\approx 0.5 \times 10^{-4}$ ,  $\approx 0.5 \times 10^{-4}$  for  $\text{He}_\alpha$ ,  $\text{Ly}_\alpha$ ,  $\text{Ly}_\beta$ ,  $\text{He}_\beta$  respectively. These values are comparable with results reported by other research groups. For example, in experiments with Ag/Cu foils [40, 41] carried out at the same laser facility but under slightly different conditions, values of  $1\text{--}2 \times 10^{-4}$  were obtained for the spectral lines Ag  $\text{K}_\alpha$  ( $E_{ph} = 22.4 \text{ keV}$ ,  $\lambda = 0.553 \text{ \AA}$ ) and Cu  $\text{K}_\alpha$  ( $E_{ph} = 1.54 \text{ keV}$ ,  $\lambda = 8.04 \text{ \AA}$ ).

#### 4. Conclusions

The laser plasma produced by the sub-PW (1 ps, 210 J, 210 TW, with focal spot diameter 7  $\mu\text{m}$ , and on target intensity  $3 \times 10^{20} \text{ W cm}^{-2}$ , angle of incidence is  $45^\circ$ ) laser pulse in a 2  $\mu\text{m}$  thick Si foil is a very bright source of soft x-rays. In the direction close to the target normal we registered emissivity of  $\approx 8 \times 10^{13} \text{ photons sr}^{-1}$  ( $\approx 0.03 \text{ J sr}^{-1}$ ) in the wavelength range of 4.75–7.3 Å (1.7–2.6 keV), which corresponds to the CE of  $\approx 1.2 \times 10^{-4} \text{ sr}^{-1}$ . About half of the energy was emitted in Si XIV ( $\text{Si}^{13+}$ )  $\text{Ly}_\alpha$ ,  $\text{Ly}_\beta$  and Si XIII ( $\text{Si}^{12+}$ )  $\text{He}_\alpha$  and  $\text{He}_\beta$  resonance spectral lines and its dielectronic satellites.  $\text{Ly}_\alpha$  line



is the most intense spectral line containing about a half of all emitted photons. This makes the  $Ly_{\alpha}$  line the best choice for quasi-monochromatic x-ray backlighter imaging and is sufficiently bright for use in appoint-project Bragg crystal imaging system.

The emissivity of the source in continuous emission in direction close to the target normal is  $\approx 13.6 \text{ mJ sr}^{-1}$  ( $CE \approx 0.7 \times 10^{-4}$ ). Approximately  $5 \text{ mJ sr}^{-1}$  ( $CE \approx 0.25 \times 10^{-4}$ ) of it corresponds to free-free (bremsstrahlung and synchrotron) radiation. The rest is associated with recombination continuum emission. Such a high value of emissivity in this type of continuous emission together with an absence of spectral lines makes the investigated source very suitable for absorption spectroscopy purposes. The value of  $CE_{4\pi}$  (a ratio between the energy emitted by the source in the full solid angle  $4\pi$  and the energy of the laser pulse) in free-free emission, estimated on the base of the simulated angular distribution and the experimentally measured emissivity, is  $1.6 \times 10^{-4}$ . This is three times less than the value obtained directly from the code EPOCH. The difference of less than one order leads to the conclusion that the code reproduces processes at the interaction point quite well.

### Data availability statement

The data that support the findings of this study are available upon reasonable request from the authors.

### Acknowledgments

The work was performed in the period from December 2019 to August 2021. The authors would like to thank the Central Laser Facility staff, whose dedication and expertise were essential to the success of their experiment. Calculations were carried out on the computational resources of the JSCC RAS. The reported study was funded by RFBR, Project Number

19-32-60050. This study was done in the frame of the State Assignment to JIHT RAS (topic #075-00892-20-00). The work of UK team received financial support from UK EPSRC Grants EP/P026796/1, EP/L01663X/1 and EP/H012605/1.

### Appendix A. Recalculation of raw data counts to number of real photons

Raw data recorded by the Fuji BAS TR IPs detectors in the experiments is a 2D matrix of numbers. Each of them is proportional to a dose absorbed by a certain pixel of the detector. This matrix can be represented in a form of a grayscale image shown in figure A1. The spectrum is a profile along the bright narrow field in the centre of the image. This zone has a non-zero width in pixels, so each dot of the spectrum is a sum along the vertical axis.

The data from IPs were digitized via Fujifilm FLA 5100 scanner. A raw image produced as a result of scanning is scaled in arbitrary units (counts), which are related with absolute units called PSL (Photostimulated Luminescence) by the equation (A.1) [42]:

$$PSL = \left( \frac{R}{100} \right)^2 \left( \frac{400}{S} \right) 10^{L \left( \frac{G}{2^B - 1} - \frac{1}{2} \right)}, \quad (\text{A.1})$$

where  $R$  is the resolution in microns,  $S$  is a sensitivity setting,  $L$  is the latitude,  $B$  is a dynamic range in bits,  $G$  is the raw image grayscale value, which is sometimes mentioned as a quantum yield. We used the following values for scanning:  $R = 25$ ,  $S = 5000$ ,  $L = 5$ ,  $B = 16$ . It should be noted that the counts-to-PSL recalculation function can be significantly different for other scanner models. For example, for General Electric Typhoon FLA 7000 the equation can be found in [43]. The values in PSL were recalculated to a number of photons with a given wavelength on the base of a calibration curve shown in figure A2.

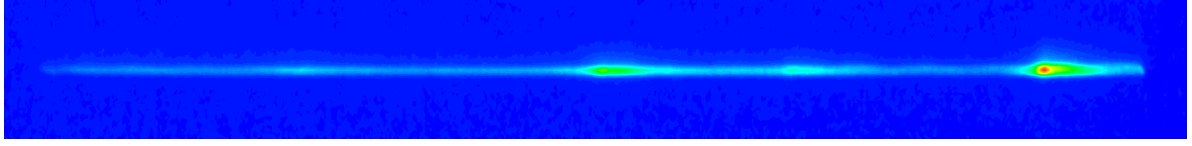


**Figure A1.** An example of an experimental x-ray emission spectrum registered by the IP detector installed in the FSSR.

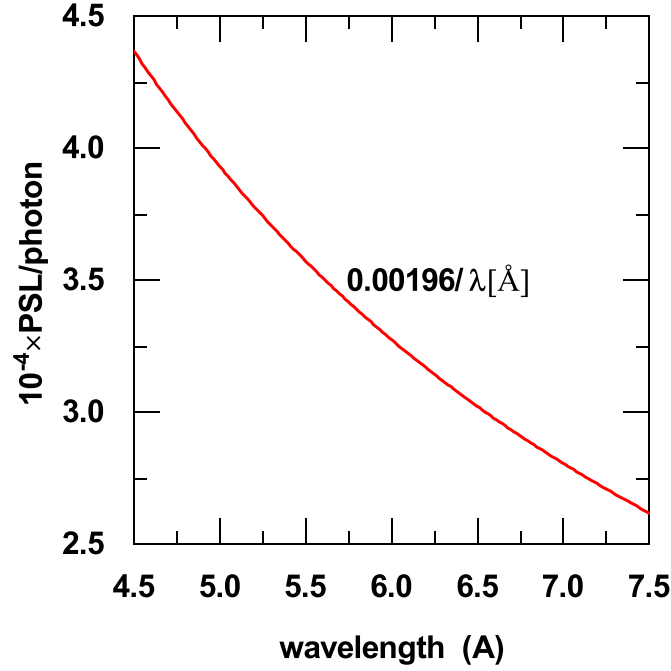


**Figure A2.** Sensitivity of Fuji BAS TR IPs in the soft x-ray range from [42] fitted by a hyperbola function.

## Appendix B. Crystal reflectivity

The corrections associated with crystal reflectivity (CR) were also considered during spectra restoring process. The CR function here is  $N_r/N_e$ , where  $N_r$  and  $N_e$  are numbers of photons reflected by a crystal and emitted by a source, correspondingly. It depends on a solid angle covered by the spectrometer crystal ( $\Omega_{cr}$ ) and also on its rocking curves (diffraction profiles).  $\Omega_{cr}$  was calculated directly from the distance between the source and the crystals and the surface dimensions of the latter ones. Rocking curves were obtained by the

x-ray Oriented Programs (XOP) [28]. This software allowed to simulate diffraction properties of spherically-bent crystals on the base of extended dynamical theory, which is fully described, for example, in [44]. The calculated rocking curves are shown in figure B1. The curves were taken into account in a numerical simulation (modelling principles are described in [27]) of rays propagation through the spectrometers optical schemes. They were considered as profiles of probability for a photon with given energy and incidence angle to be reflected by spherically bent crystals of the FSSRs.

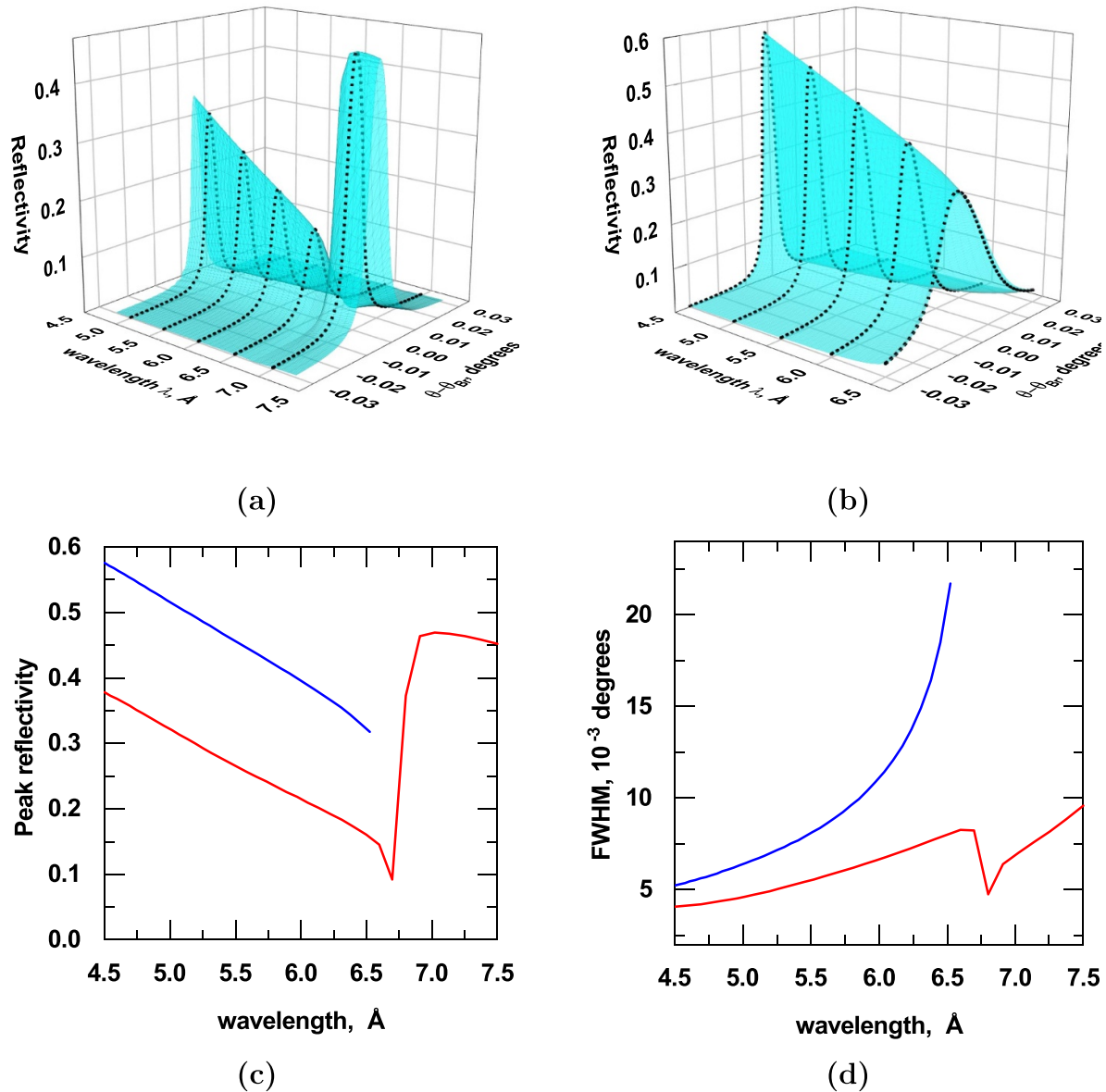


**Figure B1.** Set of rocking curves presented as a 3D surface calculated by the XOP software for spherically bent  $\alpha$ -quartz crystals with Miller indexes (a) (100) and (b) (101) for the range of wavelengths observed in the experiment. For (101) the data is not presented for  $\lambda > 6.666$  Å, because the crystal is not able to reflect photons with a wavelength longer than its interplanar spacing  $2d = 6.666$  Å. Dependence of the peaks amplitude (peak reflectivity for a particular wavelength) and FWHM are given on the planes (c) and (d) correspondingly: red line for (100), blue line for (101).

## ORCID iDs

Sergey N Ryazantsev <https://orcid.org/0000-0002-9118-7952>  
 Artem S Martynenko <https://orcid.org/0000-0001-6904-9601>  
 Igor Yu Skobelev <https://orcid.org/0000-0003-1828-2942>  
 Yaroslav S Lavrinenko <https://orcid.org/0000-0002-4604-5373>  
 Christopher D Baird <https://orcid.org/0000-0001-9973-7173>  
 Paul McKenna <https://orcid.org/0000-0001-8061-7091>  
 Christopher D Murphy <https://orcid.org/0000-0003-3849-3229>

Nigel Woolsey <https://orcid.org/0000-0002-2444-9027>  
 Sergey A Pikuz <https://orcid.org/0000-0003-2529-1142>

## References

- [1] Workman J, Maksimchuk A, Liu X, Ellenberger U, Coe J S, Chien C-Y and Umstadter D 1996 Picosecond soft-x-ray source from subpicosecond laser-produced plasmas *J. Opt. Soc. Am. B* **13** 125
- [2] Wharton K B, Boley C D, Komashko A M, Rubenchik A M, Zweiback J, Crane J, Hays G, Cowan T E and Ditmire T 2001 Effects of nonionizing prepulses in high-intensity laser-solid interactions *Phys. Rev. E* **64** 025401
- [3] Riley D, Angulo-Gareta J J, Khattak F Y, Lamb M J, Foster P S, Divall E J, Hooker C J, Langley A J, Clarke R J

- and Neely D 2005  $K_{\alpha}$  yields from Ti foils irradiated with ultrashort laser pulses *Phys. Rev. E* **71** 016406
- [4] Murnane M M, Kapteyn H C, Gordon S P, Bokor J, Glytsis E N and Falcone R W 1993 Efficient coupling of high-intensity subpicosecond laser pulses into solids *Appl. Phys. Lett.* **62** 1068–70
  - [5] Kahaly S, Yadav S K, Wang W M, Sengupta S, Sheng Z M, Das A, Kaw P K and Kumar G R 2008 Near-complete absorption of intense, ultrashort laser light by sub- $\lambda$  gratings *Phys. Rev. Lett.* **101** 145001
  - [6] Sumeruk H A, Kneip S, Symes D R, Churina I V, Belolipetski A V, Donnelly T D and Ditmire T 2007 Control of strong-laser-field coupling to electrons in solid targets with wavelength-scale spheres *Phys. Rev. Lett.* **98** 045001
  - [7] Kulcsár G, AlMawlawi D, Budnik F W, Herman P R, Moskovits M, Zhao L and Marjoribanks R S 2000 Intense picosecond x-ray pulses from laser plasmas by use of nanostructured “Velvet” targets *Phys. Rev. Lett.* **84** 5149–52
  - [8] Ovchinnikov A, Kostenko O, Chefonov O, Rosmej O, Andreev N, Agranat M, Duan J, Liu J and Fortov V 2011 Characteristic x-rays generation under the action of femtosecond laser pulses on nano-structured targets *Laser Part. Beams* **29** 249–54
  - [9] Hollinger R *et al* 2017 Efficient picosecond x-ray pulse generation from plasmas in the radiation dominated regime *Optica* **4** 1344
  - [10] Schultz K A *et al* 2019 Study of pure and mixed clustered noble gas puffs irradiated with a high intensity ( $7 \times 10^{19}$  W/cm<sup>2</sup>) sub-ps laser beam and achievement of a strong x-ray flash in a laser-generated debris-free x-ray source *Laser Part. Beams* **37** 276–87
  - [11] Kantsyrev V *et al* 2016 Study of x-rays produced from debris-free sources with Ar, Kr and Kr/Ar mixture linear gas jets irradiated by UNR Leopard laser beam with fs and ns pulse duration *High Energy Density Phys.* **19** 11–22
  - [12] Kantsyrev V L *et al* 2016 Influence of Xe and Kr impurities on x-ray yield from debris-free plasma x-ray sources with an Ar supersonic gas jet irradiated by femtosecond near-infrared-wavelength laser pulses *Phys. Rev. E* **94** 053203
  - [13] Hu G-Y *et al* 2008 Angular distribution and conversion of multi-keV L-shell x-ray sources produced from nanosecond laser irradiated thick-foil targets *Laser Part. Beams* **26** 661–70
  - [14] Rathore R, Arora V, Singhal H, Mandal T, Chakera J and Naik P 2017 Experimental and numerical study of ultra-short laser-produced collimated Cu K  $\alpha$  x-ray source *Laser Part. Beams* **35** 442–9
  - [15] Kleine C *et al* 2019 Soft x-ray absorption spectroscopy of aqueous solutions using a table-top femtosecond soft x-ray source *J. Phys. Chem. Lett.* **10** 52–58
  - [16] Khan S F *et al* 2021 A dual high-energy radiography platform with 15  $\mu$ m resolution at the national ignition facility *Rev. Sci. Instrum.* **92** 043712
  - [17] Casner A *et al* 2015 LMJ/PETAL laser facility: overview and opportunities for laboratory astrophysics *High Energy Density Phys.* **17** 2–11
  - [18] National Academies of Sciences, Engineering and Medicine 2018 *Opportunities in Intense Ultrafast Lasers: Reaching for the Brightest Light* (Washington, DC: National Academies Press) (<https://doi.org/10.17226/24939>)
  - [19] Sangster T C *et al* 2007 Cryogenic DT and D2 targets for inertial confinement fusion *Phys. Plasmas* **14** 058101
  - [20] Stoeckl C *et al* 2014 Soft x-ray backlighting of cryogenic implosions using a narrowband crystal imaging system (invited) *Rev. Sci. Instrum.* **85** 11E501
  - [21] McGuffey C *et al* 2018 Soft x-ray backlighter source driven by a short-pulse laser for pump-probe characterization of warm dense matter *Rev. Sci. Instrum.* **89** 10F122
  - [22] Martynenko A S *et al* 2021 Optimization of a laser plasma-based x-ray source according to WDM absorption spectroscopy requirements *Matter Radiat. Extremes* **6** 014405
  - [23] Loupiaz B, Perez F, Benuzzi-Mounaix A, Ozaki N, Rabec M, Gloahec L, Pikuz T, Faenov A, Aglitskiy Y and Koenig M 2009 Highly efficient, easily spectrally tunable x-ray backlighting for the study of extreme matter states *Laser Part. Beams* **27** 601–9
  - [24] Danson C *et al* 2004 Vulcan petawatt—an ultra-high-intensity interaction facility *Nucl. Fusion* **44** S239–46
  - [25] Scott G G *et al* 2015 Optimization of plasma mirror reflectivity and optical quality using double laser pulses *New J. Phys.* **17** 033027
  - [26] Faenov A Y, Pikuz S A, Erko A I, Bryunetkin B A, Dyakin V M, Ivanenkov G V, Mingaleev A R, Pikuz T A, Romanova V M and Shelkovenko T A 1994 High-performance x-ray spectroscopic devices for plasma microsources investigations *Phys. Scr.* **50** 333–8
  - [27] Lavrinenko Y S, Morozov I V, Pikuz S A and Skobelev I Y 2015 Reflectivity and imaging capabilities of spherically bent crystals studied by ray-tracing simulations *J. Phys.: Conf. Ser.* **653** 012027
  - [28] Sánchez del Río M and Dejus R J 2011 XOP v2.4: recent developments of the x-ray optics software toolkit *Proc. SPIE* **8141** 814115
  - [29] Henke B, Gullikson E and Davis J 1993 X-ray interactions: photoabsorption, scattering, transmission and reflection at  $E = 50$ –30,000 eV,  $Z = 1$ –92 At. *Data Nucl. Data Tables* **54** 181–342
  - [30] Li D, Bancroft G, Fleet M and Feng X H 1995 Silicon K-edge XANES spectra of silicate minerals *Phys. Chem. Miner.* **22** 115–22
  - [31] Macfarlane J J, Golovkin I E, Woodruff P R, Welch D R, Oliver B V, Melhorn T A and Campbell R B 2004 Simulation of the ionization dynamics of aluminum irradiated by intense short-pulse lasers *Inertial Fusion Sciences and Applications 2003 (IFSA 2003): State of the Art 2003* ed B A Hammel, D Meyerhofer, J Meyer-ter Vehn and H Azechi (La Grange Park, IL: American Nuclear Society) p 457
  - [32] Hoarty D J *et al* 2013 Observations of the effect of ionization-potential depression in hot dense plasma *Phys. Rev. Lett.* **110** 265003
  - [33] Hummer D G and Mihalas D 1988 The equation of state for stellar envelopes. I—an occupation probability formalism for the truncation of internal partition functions *Astrophys. J.* **331** 794
  - [34] Arber T D *et al* 2015 Contemporary particle-in-cell approach to laser-plasma modelling *Plasma Phys. Control. Fusion* **57** 113001
  - [35] Raizer Y 1991 *Gas Discharge Physics* (Berlin: Springer)
  - [36] Landau L D and Lifshitz E 1985 *The Classical Theory of Fields* vol 2 (Oxford: Butterworth-Heinemann)
  - [37] Vyskočil J, Klimo O and Weber S 2018 Simulations of bremsstrahlung emission in ultra-intense laser interactions with foil targets *Plasma Phys. Control. Fusion* **60** 054013
  - [38] Ducloux R, Kirk J G and Bell A R 2011 Monte Carlo calculations of pair production in high-intensity laser–plasma interactions *Plasma Phys. Control. Fusion* **53** 015009
  - [39] Elkina N V, Fedotov A M, Kostyukov I Y, Legkov M V, Narozhny N B, Nerush E N and Ruhl H 2011 QED cascades induced by circularly polarized laser fields *Phys. Rev. Spec. Top. Accel. Beams* **14** 054401
  - [40] Park H-S, Izumi N, Key M H, Koch J A, Landen O L, Patel P K, Phillips T W and Zhang B B 2004 Characteristics

- of high energy  $K\alpha$  and Bremsstrahlung sources generated by short pulse petawatt lasers *Rev. Sci. Instrum.* **75** 4048–50
- [41] Park H-S *et al* 2006 High-energy  $K\alpha$  radiography using high-intensity, short-pulse lasers *Phys. Plasmas* **13** 056309
- [42] Haugh M J, Lee J, Romano E and Schneider M 2013 Calibrating image plate sensitivity in the 700 to 5000 eV spectral energy range *Proc. SPIE* **8850** 885007
- [43] Golovin D, Mirfayzi S, Shokita S, Abe Y, Lan Z, Arikawa Y, Morace A, Pikuz T and Yogo A 2021 Calibration of imaging plates sensitivity to high energy photons and ions for laser-plasma interaction sources *J. Instrum.* **16** T02005
- [44] Authier A 2003 *Dynamical Theory of X-Ray Diffraction* (Oxford: Oxford University Press)